Unsteady drag force on an immersed sphere oscillating near a wall

Zaicheng Zhang, Vincent Bertin, Martin Essink, Hao Zhang, Nicolas Fares, Zaiyi Shen, Thomas Bickel, Thomas Salez, Abdelhamid Maali

Unsteady drag force on an immersed sphere oscillating near a wall

Zaicheng Zhang[1], Vincent Bertin[2], Martin H. Essink[2], Hao Zhang[1], Nicolas Fares[1], Zaiyi Shen[3], Thomas Bickel[1], Thomas Salez[1] † and Abdelhamid Maali[1] ‡

[1]Univ. Bordeaux, CNRS, LOMA, UMR 5798, 33405 Talence, France.

[2]Physics of Fluids Group, Faculty of Science and Technology, Mesa+ Institute, University of Twente, 7500 AE Enschede, The Netherlands.

[3]State Key Laboratory for Turbulence and Complex Systems, Department of Mechanics and Engineering Science, College of Engineering, Peking University, Beijing 100871, China

(Received xx; revised xx; accepted xx)

The unsteady hydrodynamic drag exerted on an oscillating sphere near a planar wall is addressed experimentally, theoretically, and numerically. The experiments are performed by using colloidal-probe Atomic Force Microscopy (AFM) in thermal noise mode. The natural resonance frequencies and quality factors are extracted from the measurement of the power spectrum density of the probe oscillation for a broad range of gap distances and Womersley numbers. The shift in the natural resonance frequency of the colloidal probe as the probe goes close to a solid wall infers the wall-induced variations of the effective mass of the probe. Interestingly, a crossover from a positive to a negative shift is observed as the Womersley number increases. In order to rationalize the results, the confined unsteady Stokes equation is solved numerically using a finite-element method, as well as asymptotic calculations. The in-phase and out-of-phase terms of the hydrodynamic drag acting on the sphere are obtained and agree well to the experimental results. All together, the experimental, theoretical, and numerical results show that the hydrodynamic force felt by an immersed sphere oscillating near a wall is highly dependent on the Womersley number.

Key words: Fluid mechanics, nanofluidics, colloidal-probe Atomic Force Microscopy (AFM).

1. Introduction

The motion of particles in a fluid is one of the central problems in fluid mechanics, across many scales. The hydrodynamic drag force exerted by the fluid on the particles is the fundamental quantity that dictates the motion. Applications include the sedimentation of synthetic entities, the swimming of biological microorganisms (see Wang & Ardekani 2012; Wei *et al.* 2019, 2021; Redaelli *et al.* 2022), blood flows (see Ku 1997), peristaltic pumping (see Shapiro *et al.* 1969), microfluidic flows (see Dincau *et al.* 2020), Brownian motion at short times (see Felderhof 2005; Mo & Raizen 2019), etc... At small Reynolds number, while the steady, bulk, Stokes' drag force exerted on a translating sphere is well known, addressing further the transient contributions is more intricate – even though the implications of such effects are potentially numerous.

For an isolated spherical particle with radius R translating in a viscous liquid at velocity $\boldsymbol{V}$, the bulk drag force $\boldsymbol{F}$ at small Reynolds number is given by the Basset-Boussinesq-Oseen (BBO) expression (see Basset 1888; Maxey & Riley 1983; Lovalenti & Brady 1993; Landau & Lifshitz

† Email address for correspondence: thomas.salez@cnrs.fr
‡ Email address for correspondence: abdelhamid.maali@u-bordeaux.fr

1987):

$$\boldsymbol{F} = -6\pi\eta R\boldsymbol{V} - 6R^2\sqrt{\pi\rho\eta}\int_{-\infty}^{t}\frac{1}{\sqrt{t-\tau}}\frac{\mathrm{d}\boldsymbol{V}}{\mathrm{d}\tau}\mathrm{d}\tau - \frac{2\pi\rho R^3}{3}\frac{\mathrm{d}\boldsymbol{V}}{\mathrm{d}t}, \tag{1.1}$$

where ρ and η are the density and dynamic viscosity of the viscous liquid, respectively. The right-hand side of the latter equation includes three terms successively: a Stokes viscous force, a Basset memory term, and an added-mass term. The Basset force originates from the diffusive nature of vorticity within the unsteady Stokes equation, and the added-mass force can be interpreted as an inertial effect due to the displaced fluid mass. Equation (1.1) provides a good description of particle dynamics in a large variety of particle-laden and multi-phase flows, as long as the particle Reynolds number is small (see Balachandar & Eaton 2010).

Nevertheless, the effect of nearby solid boundaries on the unsteady drag is still an open question. The canonical situation is that of an immersed sphere oscillating near a planar rigid surface. Some asymptotic expressions of the drag in the large-distance limit have been derived recently, by using a point-particle approximation together with the method of images (Felderhof 2005, 2012; Simha *et al.* 2018), or by using low or high frequency expansions of the unsteady Stokes equations (Fouxon & Leshansky 2018). However, theoretical descriptions of the confined limit, *i.e.* where the sphere is in close proximity to the surface, are scarce. We thus aim here at investigating the unsteady drag, in the full spatial range from bulk to confinement, by combining numerical simulations, asymptotic calculations and colloidal-probe Atomic Force Microscopy (AFM) experiments.

AFM colloidal-probe methods and their Surface Force Apparatus (SFA) analogues, have been first introduced in the 1990's in order to measure molecular interactions (*e.g.* electrostatic, van der Waals, ...) between surfaces (see Butt 1991; Ducker *et al.* 1991; Butt *et al.* 2005). Recently, these methods have been extended and used to study flow under micro-to-nanometric confinement, *e.g.* near soft (see Leroy & Charlaix 2011; Leroy *et al.* 2012; Villey *et al.* 2013; Guan *et al.* 2017; Zhang *et al.* 2022) or capillary interfaces (see Manor *et al.* 2008; Vakarelski *et al.* 2010; Manica *et al.* 2016; Maali *et al.* 2017; Wang *et al.* 2018; Bertin *et al.* 2021), using complex fluids (see Comtet *et al.* 2017*a*,*b*, 2019), or to measure the friction at solid-liquid interfaces (see Cottin-Bizonne *et al.* 2003; Maali *et al.* 2008; Cross *et al.* 2018), and electrohydrodynamic effects (see Liu *et al.* 2018, 2015; Zhao *et al.* 2020; Rodríguez Matus *et al.* 2022), etc... More specifically, for dynamic colloidal AFM measurements, a micron-size spherical colloidal probe is placed in a viscous fluid, in the vicinity of a surface, with a probe-surface distance D. Then, the probe is driven to oscillate without direct contact, via either acoustic excitation or thermal noise. The force exerted on the sphere is inferred from the colloidal motion, trough the cantilever's deflection, which allows to extract specific information on the confined surfaces or fluid properties. We point out that other experimental techniques were used to probe the bulk streaming flow around an oscillating sphere at finite Reynolds numbers, like particle visualization techniques (Kotas *et al.* 2007; Otto *et al.* 2008), and optical tweezers (Bruot *et al.* 2021).

If the typical angular frequency of the flow is ω, then the vorticity diffuses on a typical distance $\delta \sim \sqrt{\eta/(\rho\omega)}$ called the viscous penetration length. The dynamic force measurements are usually restricted to low Reynolds numbers, low probing frequencies, and to the confined regime where $D \ll R$. In such a case, the penetration length is large, the flow is mainly located in the confined fluid layer, it is purely viscous and quasi-steady, and the lubrication theory holds (see Reynolds 1886; Leroy & Charlaix 2011). Consequently, in all the above examples, the fluid inertial effects are disregarded in the analysis of the measured hydrodynamic force. However, when the colloidal probe oscillates at high frequencies, the penetration depth δ becomes smaller and comparable to the characteristic length scale of the flow. Thus, unsteady effects become important (see Clarke *et al.* 2005). The relevant dimensionless number to characterize the crossover to such a regime is the Womersley number $\mathrm{Wo} = R\sqrt{\omega/\nu}$, the square of which corresponds to the ratio between

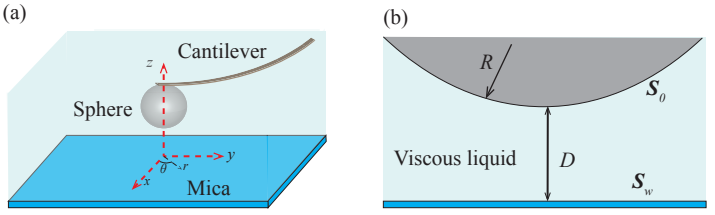

FIGURE 1. Schematics of the system. A borosilicate sphere with radius R is glued at the end of an AFM cantilever, and thermally fluctuates within a viscous liquid and near a mica substrate, with a distance D between the sphere and the substrate. The sphere and the mica surfaces are denoted as $\mathcal{S}_0$ and $\mathcal{S}_w$, respectively.

the typical diffusion time scale R^2/ν, and the period of the oscillation. Inertial effects should be predominant when it takes more time for the velocity field to diffuse than for the sphere to oscillate, *i.e.* Wo $>$ 1. In such a situation, the hydrodynamic force exerted on the sphere is not only a viscous lubrication drag, but it also contains contributions due to the fluid inertia, which were partly studied in previous works (see Sader 1998; Benmouna & Johannsmann 2002; Clarke *et al.* 2005; Devailly *et al.* 2020).

The article is organized as follows. In Sec. 2, we introduce the experimental method of thermal noise AFM and present the typical experimental results. We show that, as the distance to the wall is reduced, the natural frequency increases for low Womersley numbers but decreases for high Womersley numbers. In contrast, the dissipation monotonically increases with decreasing distance for all Womersley numbers. In order to rationalize the results, in Sec. 3, we compute the hydrodynamic drag force in terms of added mass and dissipation, in the asymptotic limit of large distance, and we perform a detailed calculation in the Low-Womersley limit using the Lorentz reciprocal theorem. Furthermore, a finite-element method is employed to obtain the full numerical solution in all regimes. Finally, the experimental, theoretical and numerical results are summarized and compared in Sec. 4. Mainly, the variation of the resonance frequency is rationalized by the change of the effective mass with distance and Womersley number.

2. Experiments

2.1. *Colloidal-probe AFM setup*

A schematic of the experimental system is shown in Fig. 1(a). A borosilicate sphere (MOSci Corporation, radius $R = 27 \pm 0.5\,\mu$m) is glued (Epoxy glue, Araldite) to the end of an AFM cantilever (SNL-10, Brukerprobes), and located near a planar mica surface. The cantilever stiffness $k_c = 0.68 \pm 0.05$ N/m is calibrated using the drainage method proposed by Craig & Neto (2001). The experiments were performed using an AFM (Bruker, Dimension3100) in three different liquids, *i.e* water, dodecane and silicone oil, whose densities and dynamic viscosities are 1000 kg/m^3, 1 mPa $\cdot$ s, 750 kg/m^3, 1.34 mPa $\cdot$ s and 930 kg/m^3, 9.3 mPa $\cdot$ s, respectively, at room temperature. The probe-surface distance D was controlled by an integrated stage step motor. Each separation distance was adjusted by displacing the cantilever vertically using the step motor with precision in position $< 0.1\,\mu$m. The probe's deflection was directly acquired using an analog to digital (A/D) acquisition card (PCI-4462, NI, USA) with a sample frequency of 200 kHz. The vertical position of the probe was observed to fluctuate due to thermal noise, as discussed in the following section. The amplitude of the sphere's fluctuation remains smaller than $\sim$ 1 nm in all the experiments.

2.2. *Confined thermal dynamics*

The time-dependent position of the probe is denoted $Z(t)$. We suppose that the probe dynamics can be modelled by a forced harmonic oscillator, as:

$$m_\infty \ddot{Z} + \gamma_\infty \dot{Z} + k_c Z = F_{th} + F_{int}, \tag{2.1}$$

where m_∞ is the effective mass of the probe in the bulk, and where γ_∞ is the bulk damping coefficient. These two coefficients correspond to the free dynamics of the probe far from the surface, and can thus be obtained by measuring the resonance properties of the AFM probe in the far field, as shown below. Besides the elastic restoring force by the cantilever of stiffness k_c, and in the absence of conservative forces (*e.g.* van der Waals or electrostatic forces), the two main forces acting on the sphere along the z direction are the random thermal force F_{th} and the hydrodynamic interaction force with the wall F_{int}. The latter corresponds to the deviation of the hydrodynamic drag with respect to the bulk drag force.

Taking the Fourier transform of Eq. (2.1), we find:

$$-m_\infty \omega^2 \tilde{Z} + i\omega\gamma_\infty \tilde{Z} + k_c \tilde{Z} = \tilde{F}_{th} + \tilde{F}_{int}, \tag{2.2}$$

where $\tilde{f}(\omega) = \frac{1}{2\pi}\int_{-\infty}^{\infty} \mathrm{d}t\, f(t) e^{-i\omega t}$ is the Fourier transform of the function $f(t)$. The real and imaginary parts of $\tilde{F}_{int}$ correspond to an inertial force and a dissipative force, respectively, that can be recast into:

$$\tilde{F}_{int} = m_{int}\omega^2 \tilde{Z} - i\omega\gamma_{int}\tilde{Z}, \tag{2.3}$$

where m_{int} and γ_{int} are the wall-induced variations of the effective mass and dissipation coefficient. For the sake of simplicity, we neglect in the following the possible frequency dependencies of m_{int} and γ_{int}. With this assumption, and injecting Eq. (2.3) into Eq. (2.2), the probe's motion follows a thermally-forced harmonic oscillator dynamics with a spring constant k_c, an effective damping coefficient $\gamma \equiv \gamma_\infty + \gamma_{int}$ and an effective mass $m \equiv m_\infty + m_{int}$. For the latter problem, one can then derive the one-sided power spectral density $S(\omega) \equiv 2\langle|\tilde{Z}(\omega)|^2\rangle$, as:

$$S(\omega) = \frac{2\langle|F_{th}|^2\rangle/(m^2\omega_0^4)}{\left[1-\left(\frac{\omega}{\omega_0}\right)^2\right]^2 + \left(\frac{\omega}{\omega_0 Q}\right)^2} = \frac{2k_B T/(\pi Q m \omega_0^3)}{\left[1-\left(\frac{\omega}{\omega_0}\right)^2\right]^2 + \left(\frac{\omega}{\omega_0 Q}\right)^2}, \tag{2.4}$$

where $\langle\cdot\rangle$ denotes the ensemble average, $k_B T$ is the thermal energy, $\omega_0 = \sqrt{k_c/(m_\infty + m_{int})}$ is the natural angular frequency, and $Q = (m_\infty + m_{int})\omega_0/\gamma$ is the quality factor. The second equality in Eq. (2.4) is obtained by using the correlator of the noise $\langle F_{th}(t)F_{th}(t')\rangle = 2\gamma k_B T \delta_D(t-t')$, where we assumed a white noise through the Dirac distribution δ_D , and where we invoked the fluctuation-dissipation theorem to set the amplitude of the noise. The experimental power spectral densities are fitted by the function (Honig *et al.* 2010; Bowles *et al.* 2011):

$$S(\omega) = \frac{c_1}{\left[1-\left(\frac{\omega}{\omega_0}\right)^2\right]^2 + \left(\frac{\omega}{\omega_0 Q}\right)^2} + c_2, \tag{2.5}$$

where ω_0 and Q are the key adjustable parameters indicating the position and the width of the resonance, and where c_1 and c_2 are unimportant extra parameters allowing to accommodate for potential spurious experimental offset and/or prefactor.

2.3. *Power spectral density*

Fig. 2 displays the power spectral densities for probes immersed in dodecane or silicone oil (water was employed as well, but the similar results are not shown here), and for a variety of

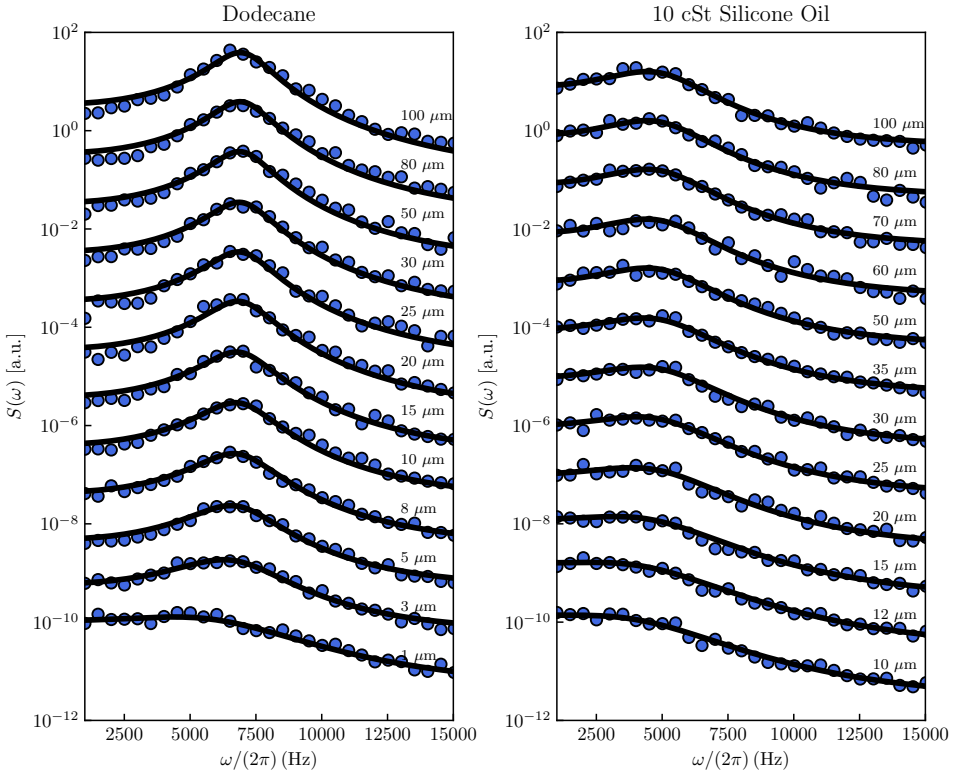

FIGURE 2. Experimental power spectral densities in arbitrary unit [a.u.], for the colloidal probe's vertical position, in dodecane (left) and silicone oil (right), for various probe-wall distances as indicated. The curves are shifted vertically for clarity. The solid lines show the best fits to the damped harmonic oscillator model, using Eq. (2.5).

probe-wall distances. A well-defined peak can be observed for each spectrum, indicating the fundamental resonance. The resonance properties are well described by the damped harmonic oscillator model above. The largest probe-wall distance ($D = 100\ \mu$m) corresponds to nearly 4 times the sphere radius, so that the hydrodynamic interactions between the probe and the wall can be neglected. At such distances, the bulk resonance frequency $\omega_0^\infty = \sqrt{k_c/m_\infty}$ and bulk quality factor $Q_\infty = m_\infty\omega_0^\infty/\gamma_\infty$ are extracted from the fitting procedure, giving respective values of 7070 ± 5 Hz and 3.3 ± 0.1 in dodecane and 5320 ± 5 Hz and 1.3 ± 0.1 in silicone oil. In the more viscous fluid (silicone oil), the resonance is broader since the dissipation is larger, as expected. Also, in both liquids, we observe that the resonance is broader as the sphere gets closer to the hard wall, which indicates that the near-wall dissipation is larger as compared to the bulk situation, as expected too. Besides, and interestingly, the natural frequency appears to depend on the viscosity of the ambient fluid, highlighting the fact that the effective mass is not trivial. Moreover, the natural frequency depends on the probe-wall distance.

To be quantitative, the fitted values of the natural frequency ω_0 and the quality factor Q are shown in Fig. 3 as functions of the normalized separation distance D/R, for the three liquids studied. Intriguingly, we observe an increase of the natural frequency in silicone oil near the wall as compared to the bulk resonance frequency (Fig. 3(a)), and a corresponding decrease in dodecane (Fig. 3(c)) and water (Fig. 3(e)). We point out that the probe-wall distances in the present experiments are large enough ($D > 0.5\ \mu$m), so that molecular interactions (*e.g.* electrostatic or van der Waals forces) can be safely neglected. Therefore, the changes in natural frequency

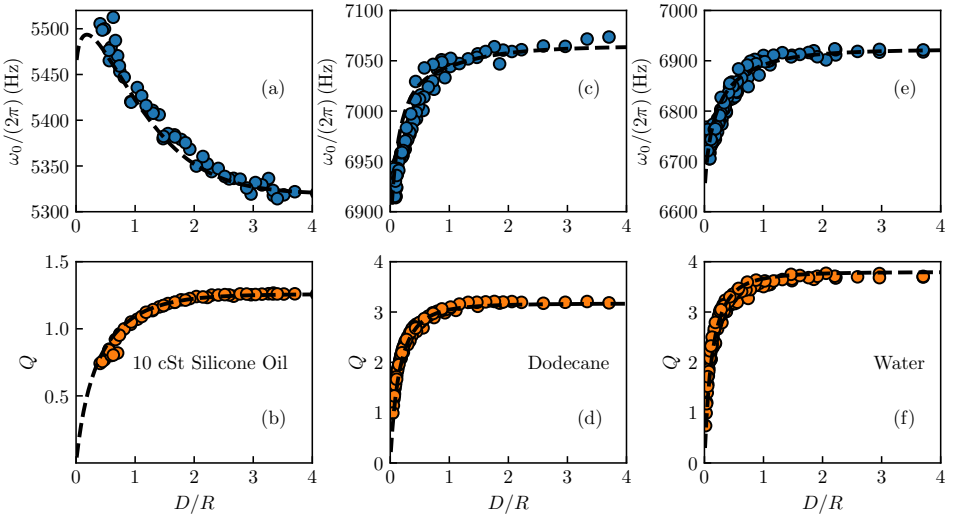

FIGURE 3. Natural frequency $\omega_0/(2\pi)$ (blue dots) and quality factor Q (orange dots) of the normal mode of the colloidal AFM probe as a function of dimensionless probe-wall distance D/R. The dashed lines represent the natural frequencies and quality factors calculated by Eq. (4.3) and Eq. (4.4), respectively without adjustable parameter. Panels (a,b) show the results for silicone oil ($\eta = 9.3$ mPa $\cdot$ s, $\rho = 930$ kg/m^3), with a squared Womersley number of $\mathrm{Wo}^2 = 2.4$. Panels (c,d) show the results for dodecane ($\eta = 1.34$ mPa $\cdot$ s, $\rho = 750$ kg/m^3), with $\mathrm{Wo}^2 = 18.1$. Panels (e,f) show the results for water ($\eta = 1$ mPa $\cdot$ s, $\rho = 1000$ kg/m^3), with $\mathrm{Wo}^2 = 31.7$.

observed here should only result from hydrodynamic contributions. The following section aims at modeling this intricate behaviour.

3. Theory

3.1. *Governing equations*

We aim here at calculating the hydrodynamic force exerted on an immersed sphere moving normally near a rigid, flat and immobile wall. The amplitude of thermal oscillations in the experiments is nanometric, which implies a relatively small Reynolds number for all accessible frequencies. Therefore, we can neglect the convective term of the incompressible Navier-Stokes equations. Nonetheless, the typical resonance frequency is in the kHz range, such that the squared Womersley number $\mathrm{Wo}^2 = R^2\omega/\nu$ is in the 1-50 range. As a consequence, we expect inertial effects to be important. The fluid velocity field $\boldsymbol{v}$ thus satisfies the unsteady incompressible Stokes equations:

$$\rho\partial_t \boldsymbol{v} = -\boldsymbol{\nabla} p + \eta\boldsymbol{\nabla}^2\boldsymbol{v}, \qquad \boldsymbol{\nabla}\cdot\boldsymbol{v} = 0\,, \tag{3.1}$$

where p is the hydrodynamic pressure field. Without loss of generality, the sphere's position is supposed to oscillate normally to the substrate at a frequency ω, and with an amplitude A, which correspond to a given Fourier mode of the full fluctuation spectrum. Applying the Fourier transform to the unsteady incompressible Stokes equations, we get:

$$i\rho\omega\tilde{\boldsymbol{v}} = -\boldsymbol{\nabla}\tilde{p} + \eta\boldsymbol{\nabla}^2\tilde{\boldsymbol{v}}, \qquad \boldsymbol{\nabla}\cdot\tilde{\boldsymbol{v}} = 0. \tag{3.2}$$

A no-slip condition is assumed at both the wall and the sphere surfaces, denoted by $\mathcal{S}_\mathrm{w}$ and $\mathcal{S}_0$ respectively (see Fig. 1 (b)), leading to the following boundary conditions for the fluid velocity

field:

$$\tilde{\boldsymbol{v}}(\boldsymbol{r} \in \mathcal{S}_0) = i\omega A \boldsymbol{e}_z\,, \qquad \tilde{\boldsymbol{v}}(\boldsymbol{r} \in \mathcal{S}_\mathrm{w}) = \boldsymbol{0}\,, \tag{3.3}$$

with $\boldsymbol{e}_z$ the unit vector in the z-direction. The hydrodynamic drag force applied on the sphere is given by:

$$\tilde{\boldsymbol{F}} = \int_{\mathcal{S}_0} \boldsymbol{n} \cdot \tilde{\boldsymbol{\sigma}}\, \mathrm{d}\mathcal{S}_0, \tag{3.4}$$

where $\tilde{\boldsymbol{\sigma}} = -\tilde{p}\mathbf{I} + \eta\left[\boldsymbol{\nabla}\tilde{\boldsymbol{v}} + (\boldsymbol{\nabla}\tilde{\boldsymbol{v}})^T\right]$ is the fluid stress tensor, and $\boldsymbol{n}$ denotes the unit vector normal to $\mathcal{S}_0$ oriented towards the fluid. To the best of our knowledge, there is no closed-form solution of the problem, in contrast with the steady case (see Brenner (1961)).

By symmetry, the drag force is directed along the z direction, *i.e.* $\tilde{\boldsymbol{F}} = \tilde{F}_z \boldsymbol{e}_z$. Using dimensional analysis, and assuming that the oscillation amplitude A is much smaller than D, one can show that the drag force $\tilde{F}_z$ normalized by the bulk Stokes reference $-6i\pi\eta RA\omega$, to form the dimensionless drag force $\tilde{f}_z = \tilde{F}_z/(-6i\pi\eta RA\omega)$, depends only on two dimensionless parameters: i) the Womersley number Wo, and ii) the sphere-wall distance relative to the sphere radius D/R. As a consequence, the dimensionless hydrodynamic interaction force (see Section 2.2 and Eq. (2.3)) reads:

$$\frac{\tilde{F}_\mathrm{int}}{6i\pi\eta RA\omega} = \tilde{f}_z\left(D/R \to \infty, \mathrm{Wo}\right) - \tilde{f}_z\left(D/R, \mathrm{Wo}\right) = \frac{(m_\mathrm{int}\omega^2 - i\omega\gamma_\mathrm{int})\tilde{Z}}{6i\pi\eta RA\omega}. \tag{3.5}$$

Although there is no general analytical solution of Eq. (3.2) with the boundary conditions of Eq. (3.3), the hydrodynamic drag force has known asymptotic expressions in certain limits, some of which are given in the next two subsections.

3.2. *Large-distance regime*

In the infinite-distance limit, the force expression reduces to the BBO equation (see Eq. (1.1)) for a sphere in an unbounded space, which gives in Fourier space:

$$\tilde{F}_z = -6i\pi\eta RA\omega\left(1 + \sqrt{-i}\mathrm{Wo} - \frac{i\mathrm{Wo}^2}{9}\right), \qquad \text{for } \; D/R \to \infty. \tag{3.6}$$

The last term of Eq. (3.6) corresponds to an inertial force of added mass $2\pi\rho R^3/3$ and the $\sqrt{-i\mathrm{Wo}}$ term corresponds to the Basset force. The large-distance asymptotic correction to the added-mass contribution due to a rigid wall has been computed using the potential-flow theory, and gives $2\pi\rho R^3\{1 + 3R^3/[8(R+D)^3]\}/3$ (see Lamb (1932)). By using a boundary-integral formulation of the unsteady incompressible Stokes equations, Fouxon & Leshansky (2018) have generalized the latter result by including the Basset force, to obtain large-distance the asymptotic drag force, that reads:

$$\tilde{F}_z = -6i\pi\eta RA\omega\left(1 + \sqrt{-i}\mathrm{Wo} - \frac{i\mathrm{Wo}^2}{9} + B\frac{R^3}{(D+R)^3}\right), \qquad \text{for } \; D/R \gg 1, \tag{3.7}$$

where the numerical prefactor B depends on Wo and reads:

$$B = \frac{1}{4}\left(1 + \sqrt{-i}\mathrm{Wo} - \frac{i\mathrm{Wo}^2}{3}\right)\left[\frac{1}{3} + \frac{3i}{2\mathrm{Wo}^2}\left(1 + \sqrt{-i}\mathrm{Wo} - \frac{i\mathrm{Wo}^2}{9}\right)\right]. \tag{3.8}$$

3.3. *Small-distance regime*

In the limit of small sphere-wall distance, which is of importance for colloidal-probe experiments, the drag force is usually dominated by viscous effects. The out-of-phase component of the force can be described by lubrication theory (see Batchelor (1967)), in which the main

contribution to the drag comes from the confined region between the sphere and the wall, which leads to the expression:

$$\tilde{F}_z = -\frac{6i\pi\eta R^2 A\omega}{D}. \tag{3.9}$$

We stress that the in-phase correction to the latter is still unknown in the lubricated limit. It would be interesting to perform asymptotic-matching calculations on the unsteady Stokes equations (see Cox & Brenner (1967)) to obtain a self-consistent expression of the effective added-mass in this limit.

3.4. *Low-Womersley-number regime*

As pointed out by Fouxon & Leshansky (2018), in the small-frequency limit, which corresponds to a small Womersley number, the drag force can be expressed in terms of known integrals, by using the Lorentz reciprocal theorem (see Masoud & Stone (2019); Fouxon *et al.* (2020)). We provide here an alternative derivation of this result.

We introduce the model steady problem of a sphere moving normally to a surface in a viscous fluid, which corresponds to the problem of Section 3.1, at zero frequency, *i.e.*:

$$\boldsymbol{\nabla}\cdot\hat{\boldsymbol{\sigma}} = \mathbf{0}\,, \qquad \boldsymbol{\nabla}\cdot\hat{\boldsymbol{v}} = 0\,, \tag{3.10}$$

with the same boundary conditions:

$$\hat{\boldsymbol{v}}(\boldsymbol{r}\in\mathcal{S}_0) = i\omega A\boldsymbol{e}_z\,, \qquad \hat{\boldsymbol{v}}(\boldsymbol{r}\in\mathcal{S}_w) = \mathbf{0}\,, \tag{3.11}$$

where $\hat{\boldsymbol{\sigma}}$ and $\hat{\boldsymbol{v}}$ are the fluid stress and velocity fields of the model problem, respectively. Integrating the Lorentz identity $\nabla\cdot(\tilde{\boldsymbol{\sigma}}\cdot\hat{\boldsymbol{v}} - \hat{\boldsymbol{\sigma}}\cdot\tilde{\boldsymbol{v}}) = i\omega\rho\tilde{\boldsymbol{v}}\cdot\hat{\boldsymbol{v}}$ on the total fluid volume, we obtain:

$$(i\omega A\boldsymbol{e}_z)\cdot\left[\int_{\mathcal{S}_0}\hat{\boldsymbol{\sigma}}\cdot\boldsymbol{n}\,\mathrm{d}\mathcal{S}_0 - \int_{\mathcal{S}_0}\tilde{\boldsymbol{\sigma}}\cdot\boldsymbol{n}\,\mathrm{d}\mathcal{S}_0\right] = i\omega\rho\int_{\mathcal{V}}\tilde{\boldsymbol{v}}\cdot\hat{\boldsymbol{v}}\,\mathrm{d}\mathcal{V}, \tag{3.12}$$

where the divergence theorem has been used. Recalling Eq. (3.4), we get:

$$\tilde{F}_z = \hat{F}_z - \frac{\rho}{A}\int_{\mathcal{V}}\tilde{\boldsymbol{v}}\cdot\hat{\boldsymbol{v}}\,\mathrm{d}\mathcal{V}. \tag{3.13}$$

The force $\hat{F}_z$ and velocity field $\hat{\boldsymbol{v}}$ of the model problem correspond to the ones derived analytically by Brenner (1961), using a modal decomposition. The force of the model problem thus reads:

$$\frac{\hat{F}_z}{6i\pi\eta R\omega A} = \frac{4}{3}\sinh(\alpha)\sum_{n=1}^{\infty}\frac{n(n+1)}{(2n-1)(2n+3)}\left\{1 - \frac{2\sinh[(2n+1)\alpha] + (2n+1)\sinh(2\alpha)}{\left[2\sinh\left((n+\tfrac{1}{2})\alpha\right)\right]^2 - [(2n+1)\sinh(\alpha)]^2}\right\}, \tag{3.14}$$

with $\cosh(\alpha) = 1 + D/R$. Nevertheless, the unsteady velocity field $\tilde{\boldsymbol{v}}$ in Eq. (3.13) is still unknown, so that the drag force $\tilde{F}_z$ cannot be found exactly.

Analytical progress can be made in the low-Wo regime, where the unsteady velocity field can be approximated by the steady solution with $O(\mathrm{Wo}^2)$ corrections, as $\tilde{\boldsymbol{v}} = \hat{\boldsymbol{v}}\left[1 + O(\mathrm{Wo}^2)\right]$. In this limit, at leading order in inertial contributions, the drag force reduces to:

$$\tilde{F}_z = \hat{F}_z - \frac{\rho}{A}\int_{\mathcal{V}}\hat{\boldsymbol{v}}^2\,\mathrm{d}\mathcal{V}. \tag{3.15}$$

The volume integral in Eq. (3.15) can then be evaluated numerically using the model velocity field provided by Brenner (1961).

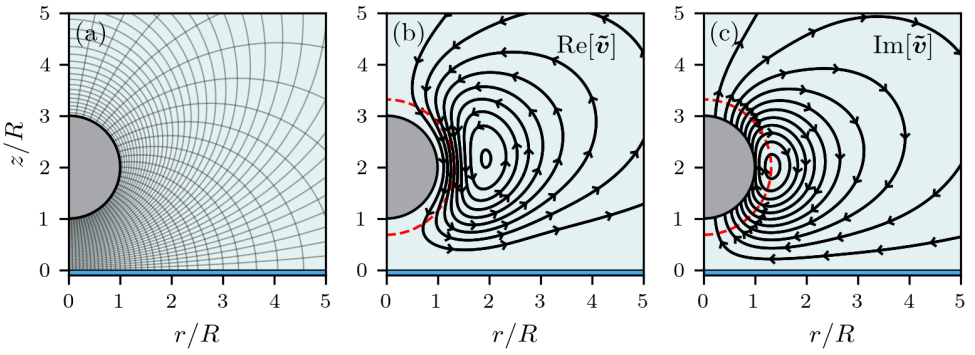

FIGURE 4. (a) Typical mesh used in the finite-element method. (b) Streamlines of the in-phase flow field, obtained numerically. (c) Streamlines of the out-of-phase flow field, obtained numerically. The squared Womersley number is set to $\mathrm{Wo}^2 = 10$, such that $\delta \approx 0.31R$. The red dashed lines indicate a sphere of radius $R + \delta$.

3.5. *Finite-element method*

We complement the previous asymptotic expressions of the drag force with full numerical solutions. Using the open-source finite-element library Nutils (see van Zwieten *et al.* (2022)), we solve Eq. (3.2). The axisymmetric velocity and pressure fields are defined on a 320×320-element mesh, uniformly spaced on a rectangular domain $[0 \leqslant \tau \leqslant \alpha,\ 0 \leqslant \sigma \leqslant \pi]$. We then use the bipolar coordinate transform:

$$r = a\frac{\sin(\sigma)}{\cosh(\tau) - \cos(\sigma)}, \qquad z = a\frac{\sinh(\tau)}{\cosh(\tau) - \cos(\sigma)}, \tag{3.16}$$

with $a = R\sinh\alpha$. The resulting mesh, when axisymmetry is considered, spans the entire domain where $r > 0$ and $z > 0$, with the exception of a circular region corresponding to the sphere, as shown in Fig. 4. On the symmetry axis ($r = 0$), the flow in the radial direction is constrained and the vertical flow is required to be shear-free. At the wall surface ($z = 0$), the velocity field is set to zero. Finally, on the surface of the sphere, the radial and vertical velocity components are set to zero and unity (imaginary part) respectively, following Eq. (3.3). From the calculated velocity and pressure fields, the total force exerted on the particle can be directly computed using Eq. (3.4). Typical flow fields are shown in Fig. 4(b) and (c).

4. Results

4.1. *Drag force*

The total hydrodynamic force is decomposed in its in-phase and out-of-phase parts, as $\tilde{F}_z = mA\omega^2 - i\gamma A\omega$, and shown in Fig. 5 and Fig. 6 versus the dimensionless sphere-wall distance. First, the Basset-Boussinesq-Oseen force of Eq. (3.6) agrees well with the simulation results at large distance, for all Wo. The infinite-distance rescaled effective mass is found to increase with decreasing Womersley number as $\sim 1/\mathrm{Wo}$, for $\mathrm{Wo}^2 \ll 1$. This effect arises from the Basset term in Eq. (3.6). Indeed, invoking the velocity scale $A\omega$, one finds a Basset force that scales as $R^2\sqrt{\rho\eta\omega}A\omega \sim \rho R^3 A\omega^2/\mathrm{Wo}$. This could rationalize the experimental observations made in Fig. 2, where the large-distance natural frequency of the colloidal probe changes in liquids of different viscosities. Conversely, the rescaled damping coefficient increases with increasing Womersley number as Wo, for $\mathrm{Wo}^2 \gg 1$ (see Fig. 6). Here again, this effect originates from the Basset force that also scales as $\eta RA\omega\mathrm{Wo}$.

Interestingly, the behaviour of the rescaled effective mass with dimensionless distance is

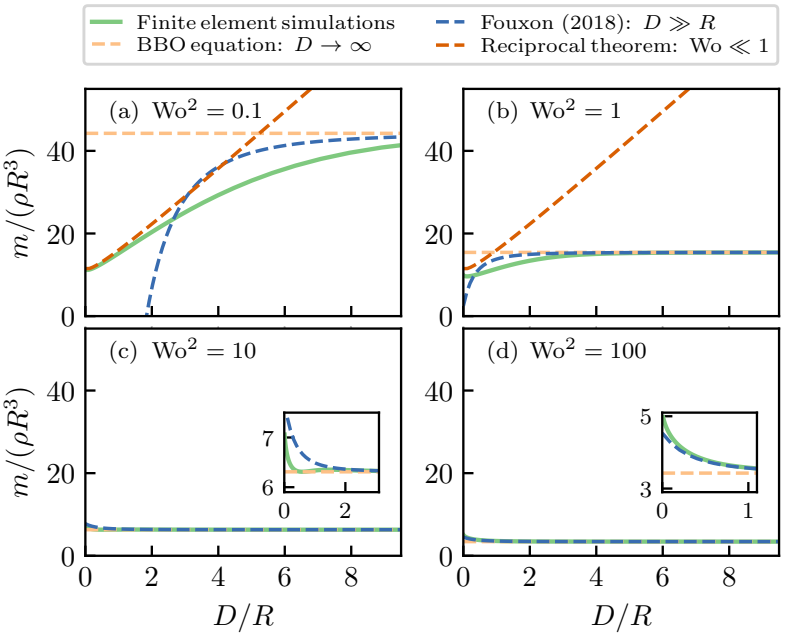

FIGURE 5. Real part of the total hydrodynamic force, normalized by the inertial force scale, $\mathrm{Re}[\tilde{F}_z]/(\rho R^3 A\omega^2) = m/(\rho R^3)$, as a function of the normalized sphere-wall distance D/R. The four panels (a-d) correspond to different Womersley numbers, as indicated. The numerical solutions of section 3.5 are shown with solid lines. The bulk Basset–Boussinesq–Oseen force of Eq. (3.6) is displayed with light orange dashed lines. The large-distance asymptotic expression of Eq. (3.7) is shown with dashed blue lines. The low-Wo expansion of Eq. (3.15) is shown with a dark orange dashed line in panel (a). The insets in panels (c) and (d) show zooms near the wall.

not universal. For large Wo, the rescaled effective mass decreases with increasing normalized distance. Furthermore, the large-distance asymptotic expression of Eq. (3.7) accurately describes the rescaled effective mass in the $\mathrm{Wo}^2 \gg 1$ regime. Indeed, Eq. (3.7) is valid as long as the sphere-wall distance exceeds the viscous penetration length, *i.e.* $D \gg \delta = R/\mathrm{Wo}$. Near the wall, deviations of the rescaled effective mass from the large-distance asymptotic expression are systematically observed (see insets in Fig. 5 (c) and (d)), and are comparable to ~ 1 in magnitude. In sharp contrast, for small Wo, the rescaled effective mass decreases with decreasing dimensionless distance. The typical Wo value at which the effective-mass variation with distance changes sign is $\mathrm{Wo}^2 \approx 5$. In addition, in the small-Wo regime, the numerical solution agrees well with the asymptotic expression of Eq. (3.15) (see Fig. 5(a)) at small dimensionless distances. Eventually, at vanishing sphere-wall distances, the effective mass tends towards a constant value, found numerically to be:

$$m \approx 11.45\rho R^3, \qquad \text{for } D \ll R \ll \delta. \tag{4.1}$$

Furthermore, an intermediate regime where the rescaled effective mass increases in an affine manner with the dimensionless distance is observed in Fig. 5(a), as predicted by Fouxon & Leshansky (2018), as:

$$m = \frac{9\pi}{4}\rho R^2(R + D), \qquad \text{for } R \ll D \ll \delta. \tag{4.2}$$

The latter asymptotic expression has been obtained by considering the Lorentz correction to the Stokes drag at large distance (see Lorentz (1907); Happel & Brenner (1983)).

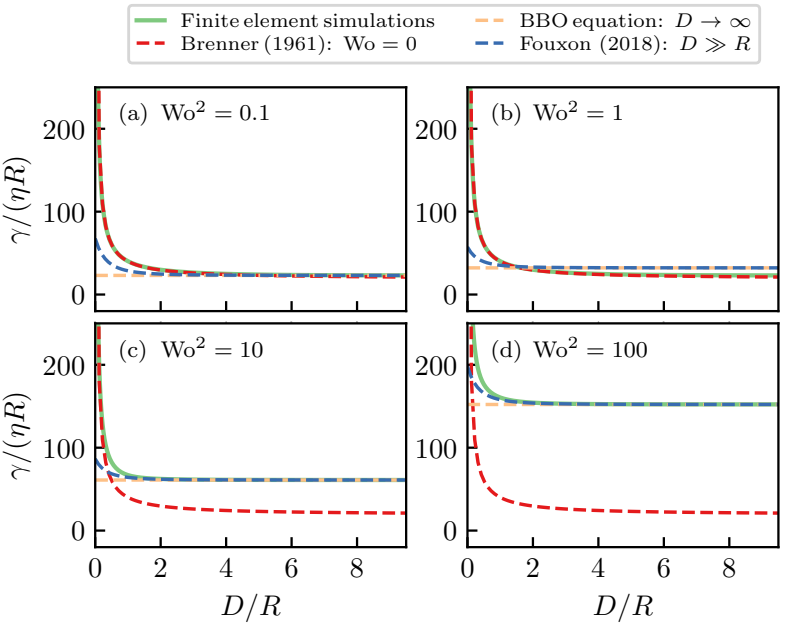

FIGURE 6. Opposite of the imaginary part of the total hydrodynamic force, normalized by the viscous force scale, $-\mathrm{Im}[\tilde{F}_z]/(\eta R A\omega) = \gamma/(\eta R)$, as a function of the normalized sphere-wall distance D/R. The four panels (a-d) correspond to different Womersley numbers, as indicated. The numerical solutions of section 3.5 are shown with solid lines. The bulk Basset–Boussinesq–Oseen force of Eq. (3.6) is displayed with light orange dashed lines. The large-distance asymptotic expression of Eq. (3.7) is shown with dashed blue lines. The viscous solution of Eq. (3.14) is shown with red dashed lines.

The rescaled damping coefficient decreases with increasing dimensionless distance (see Fig. 6). At low Wo, which corresponds to the low-frequency regime, the rescaled damping coefficient is well described at all distances by the steady drag force of Eq. (3.14). However, at large Wo, we observe a transition from the BBO expression at large distance to the steady drag force at small distance. The typical distance at which the transition occurs is $D \simeq \delta$, which is smaller than R. In this regime, the rescaled damping coefficient diverges as $\sim 1/D$, as predicted by lubrication theory (see Eq. (3.9)).

4.2. *Comparison of the model with experiments*

We now turn to a comparison of the model with experiments. The resonance properties of the colloidal probe are quantified by the natural frequency $\omega_0/(2\pi)$ and quality factor Q, as measured by fitting the power spectral density to the harmonic-oscillator model (see Section 2.3). The resulting values of these two quantities were already shown in Fig. 3, as functions of the probe-wall distance, for three different liquids of various kinematic viscosities.

Since the natural frequency variations are small, typically on the order of 5% or less of the bulk natural frequency, we perform a Taylor expansion of the natural frequency at first order in $m_{\mathrm{int}}/m_\infty$:

$$\omega_0 = \sqrt{\frac{k_c}{m_\infty + m_{\mathrm{int}}}} \simeq \omega_0^\infty \left(1 - \frac{m_{\mathrm{int}}}{2m_\infty}\right). \tag{4.3}$$

We then compute the natural frequency at all distances from the numerical simulations, by using Eq. (3.5). The Womersley number is set by using the bulk natural frequency, through $\mathrm{Wo}^2 = R^2\omega_0^\infty/\nu$. The resulting Wo^2 values are 2.4, 18.1 and 31.7 for silicone oil, dodecane

and water, respectively. As shown in Fig. 3(a)-(c)-(e), the experimental results agree with the numerical simulation, which confirms that the modification of the natural frequency of the oscillator originates from the hydrodynamic interactions between the sphere and the wall.

Similarly, we invoke an approximate expression of the quality factor:

$$Q = \frac{Q_\infty}{\frac{\omega_0}{\omega_\infty}\left(1 + \frac{\gamma_{\rm int} Q_\infty \omega_0^\infty}{k_{\rm c}}\right)} \simeq \frac{Q_\infty}{\left(1 + \frac{\gamma_{\rm int} Q_\infty \omega_0^\infty}{k_{\rm c}}\right)}. \tag{4.4}$$

We then compute the quality factor at all distances from the numerical simulations, by using Eq. (3.5), and setting the same Wo values as given above. As shown in Fig. 3(b)-(d)-(f), the experimental results agree with the numerical simulation, confirming that the decrease of the quality factor is essentially due to the increase of the viscous Stokes drag as the sphere-wall distance is reduced.

5. Conclusion

We investigated the hydrodynamic force exerted on an immersed sphere oscillating normally to a rigid planar wall, by using a combination of colloidal-probe AFM experiments, finite-element simulations and asymptotic calculations. The in-phase and out-of-phase components of the hydrodynamic force are obtained from the measurements of the natural frequency and damping of the thermal motion of the probe for various probe-wall distances. A shift in the natural frequency of the probe was observed with decreasing probe-wall distance, revealing a striking wall-induced unsteady effect: the natural frequency was found to increase with decreasing probe-wall distance in viscous liquids, whereas the opposite trend was observed in low viscosity liquids such as water. By solving the unsteady incompressible Stokes equations numerically, the hydrodynamic force was computed at all distances. The added mass and dissipation increase due to the presence of the wall were then extracted and compared to their experimental counterparts – with excellent agreement. In addition, at large distance, we recovered the analytical expression derived by Fouxon & Leshansky (2018). Besides, in the low-Womersley-number limit, the hydrodynamic force could be expressed in a simple integral form using the Lorentz reciprocal theorem, which was validated by the numerical simulations. Beneath the fundamental interest for confined or interfacial fluid dynamics, the present results might be of practical importance for colloidal experiments, because they clarify the hydrodynamic drag acting on a spherical particle near a wall. Essentially, our findings highlight the crucial but overlooked role played by fluid inertia, despite the typically low Reynolds numbers.

Acknowledgments

The authors thank Elie Raphaël, Yacine Amarouchene and Jacco Snoeijer for interesting discussions, as well as Arno Goudeau for preliminary experiments.

Funding

The authors acknowledge financial support from the European Union through the European Research Council under EMetBrown (ERC-CoG-101039103) grant. Views and opinions expressed are however those of the authors only and do not necessarily reflect those of the European Union or the European Research Council. Neither the European Union nor the granting authority can be held responsible for them. The authors also acknowledge financial support from the Agence Nationale de la Recherche under EMetBrown (ANR-21-ERCC-0010-01), Softer (ANR-21-CE06-0029), Fricolas (ANR-21-CE06-0039) and EDDL (ANR-19-CE30-0012) grants, and

from the NWO through the VICI Grant No. 680-47-632. They also acknowledge the support from the LIGHT S&T Graduate Program (PIA3 Investment for the Future Program, ANR-17-EURE-0027). Finally, they thank the Soft Matter Collaborative Research Unit, Frontier Research Center for Advanced Material and Life Science, Faculty of Advanced Life Science at Hokkaido University, Sapporo, Japan.

Declaration of Interests

The authors report no conflict of interest.

REFERENCES

Balachandar, S & Eaton, John K 2010 Turbulent dispersed multiphase flow. *Annual review of fluid mechanics* **42**, 111–133.

Basset, AB 1888 A treatise on hydrodynamics vol 2 (cambridge: Deighton, bell and co.) .

Batchelor, George Keith 1967 *An introduction to fluid dynamics*. Cambridge University Press.

Benmouna, F & Johannsmann, Diethelm 2002 Hydrodynamic interaction of afm cantilevers with solid walls: An investigation based on afm noise analysis. *The European Physical Journal E* **9**, 435–441.

Bertin, Vincent, Zhang, Zaicheng, Boisgard, Rodolphe, Grauby-Heywang, Christine, Raphaël, Elie, Salez, Thomas & Maali, Abdelhamid 2021 Contactless rheology of finite-size air-water interfaces. *Physical Review Research* **3** (3), L032007.

Bowles, Adam P, Honig, Christopher DF & Ducker, William A 2011 No-slip boundary condition for weak solid- liquid interactions. *The Journal of Physical Chemistry C* **115** (17), 8613–8621.

Brenner, Howard 1961 The slow motion of a sphere through a viscous fluid towards a plane surface. *Chemical engineering science* **16** (3-4), 242–251.

Bruot, Nicolas, Cicuta, Pietro, Bloomfield-Gadêlha, Hermes, Goldstein, Raymond E, Kotar, Jurij, Lauga, Eric & Nadal, François 2021 Direct measurement of unsteady microscale stokes flow using optically driven microspheres. *Physical Review Fluids* **6** (5), 053102.

Butt, Hans-Jürgen 1991 Measuring electrostatic, van der waals, and hydration forces in electrolyte solutions with an atomic force microscope. *Biophysical journal* **60** (6), 1438–1444.

Butt, Hans-Jürgen, Cappella, Brunero & Kappl, Michael 2005 Force measurements with the atomic force microscope: Technique, interpretation and applications. *Surface science reports* **59** (1-6), 1–152.

Clarke, Richard John, Cox, Stephen Michael, Williams, PM & Jensen, OE 2005 The drag on a microcantilever oscillating near a wall. *Journal of Fluid Mechanics* **545**, 397–426.

Comtet, Jean, Chatté, Guillaume, Nigues, Antoine, Bocquet, Lydéric, Siria, Alessandro & Colin, Annie 2017*a* Pairwise frictional profile between particles determines discontinuous shear thickening transition in non-colloidal suspensions. *Nature communications* **8** (1), 15633.

Comtet, Jean, Lainé, Antoine, Nigues, Antoine, Bocquet, Lydéric & Siria, Alessandro 2019 Atomic rheology of gold nanojunctions. *Nature* **569** (7756), 393–397.

Comtet, Jean, Niguès, Antoine, Kaiser, Vojtech, Coasne, Benoit, Bocquet, Lydéric & Siria, Alessandro 2017*b* Nanoscale capillary freezing of ionic liquids confined between metallic interfaces and the role of electronic screening. *Nature materials* **16** (6), 634–639.

Cottin-Bizonne, Cécile, Barrat, Jean-Louis, Bocquet, Lydéric & Charlaix, Elisabeth 2003 Low-friction flows of liquid at nanopatterned interfaces. *Nature materials* **2** (4), 237–240.

Cox, Raymond G & Brenner, Howard 1967 The slow motion of a sphere through a viscous fluid towards a plane surface—ii small gap widths, including inertial effects. *Chemical Engineering Science* **22** (12), 1753–1777.

Craig, Vincent SJ & Neto, Chiara 2001 In situ calibration of colloid probe cantilevers in force microscopy: hydrodynamic drag on a sphere approaching a wall. *Langmuir* **17** (19), 6018–6022.

Cross, Benjamin, Barraud, Chloé, Picard, Cyril, Léger, Liliane, Restagno, Frédéric & Charlaix, Élisabeth 2018 Wall slip of complex fluids: Interfacial friction versus slip length. *Physical Review Fluids* **3** (6), 062001.

Devailly, Clémence, Bouriat, Patrick, Dicharry, Christophe, Risso, Frédéric, Ondarçuhu, Thierry & Tordjeman, Philippe 2020 Long-range hydrodynamic forces in liquid fm-afm. *Nanotechnology* **31** (45), 455501.

Dincau, Brian, Dressaire, Emilie & Sauret, Alban 2020 Pulsatile flow in microfluidic systems. *Small* **16** (9), 1904032.

Ducker, William A, Senden, Tim J & Pashley, Richard M 1991 Direct measurement of colloidal forces using an atomic force microscope. *Nature* **353** (6341), 239–241.

Felderhof, BU 2005 Effect of the wall on the velocity autocorrelation function and long-time tail of brownian motion. *The Journal of Physical Chemistry B* **109** (45), 21406–21412.

Felderhof, BU 2012 Hydrodynamic force on a particle oscillating in a viscous fluid near a wall with dynamic partial-slip boundary condition. *Physical Review E* **85** (4), 046303.

Fouxon, Itzhak & Leshansky, Alexander 2018 Fundamental solution of unsteady stokes equations and force on an oscillating sphere near a wall. *Physical Review E* **98** (6), 063108.

Fouxon, Itzhak, Rubinstein, Boris, Weinstein, Oleg & Leshansky, Alexander 2020 Fluid-mediated force on a particle due to an oscillating plate and its effect on deposition measurements by a quartz crystal microbalance. *Physical Review Letters* **125** (14), 144501.

Guan, Dongshi, Charlaix, Elisabeth, Qi, Robert Z & Tong, Penger 2017 Noncontact viscoelastic imaging of living cells using a long-needle atomic force microscope with dual-frequency modulation. *Physical Review Applied* **8** (4), 044010.

Happel, John & Brenner, Howard 1983 *Low Reynolds number hydrodynamics: with special applications to particulate media*, , vol. 1. Springer Science & Business Media.

Honig, Christopher DF, Sader, John E, Mulvaney, Paul & Ducker, William A 2010 Lubrication forces in air and accommodation coefficient measured by a thermal damping method using an atomic force microscope. *Physical Review E* **81** (5), 056305.

Kotas, Charlotte W, Yoda, Minami & Rogers, Peter H 2007 Visualization of steady streaming near oscillating spheroids. *Experiments in fluids* **42** (1), 111–121.

Ku, David N 1997 Blood flow in arteries. *Annual review of fluid mechanics* **29** (1), 399–434.

Lamb, Horace 1932 *Hydrodynamics*. Cambridge University Press.

Landau, Lev Davidovich & Lifshitz, Evgenii Mikhailovich 1987 *Fluid Mechanics: Landau and Lifshitz: Course of Theoretical Physics, Volume 6*, , vol. 6. Oxford, England; New York: Pergamon Press,.

Leroy, Samuel & Charlaix, Elisabeth 2011 Hydrodynamic interactions for the measurement of thin film elastic properties. *Journal of Fluid Mechanics* **674**, 389–407.

Leroy, Samuel, Steinberger, Audrey, Cottin-Bizonne, Cécile, Restagno, Frédéric, Léger, Liliane & Charlaix, Elisabeth 2012 Hydrodynamic interaction between a spherical particle and an elastic surface: a gentle probe for soft thin films. *Physical review letters* **108** (26), 264501.

Liu, F, Klaassen, A, Zhao, C, Mugele, F & Van Den Ende, D 2018 Electroviscous dissipation in aqueous electrolyte films with overlapping electric double layers. *The Journal of Physical Chemistry B* **122** (2), 933–946.

Liu, Fei, Zhao, Cunlu, Mugele, Frieder & van den Ende, Dirk 2015 Amplitude modulation atomic force microscopy, is acoustic driving in liquid quantitatively reliable? *Nanotechnology* **26** (38), 385703.

Lorentz, Hendrik Antoon 1907 Ein allgemeiner satz, die bewegung einer reibenden flüssigkeit betreffend, nebst einigen anwendungen desselben. *Abh. Theor. Phys* **1**, 23.

Lovalenti, Phillip M & Brady, John F 1993 The hydrodynamic force on a rigid particle undergoing arbitrary time-dependent motion at small reynolds number. *Journal of Fluid Mechanics* **256**, 561–605.

Maali, Abdelhamid, Boisgard, Rodolphe, Chraibi, Hamza, Zhang, Zaicheng, Kellay, Hamid & Würger, Aloïs 2017 Viscoelastic drag forces and crossover from no-slip to slip boundary conditions for flow near air-water interfaces. *Physical review letters* **118** (8), 084501.

Maali, Abdelhamid, Cohen-Bouhacina, Touria & Kellay, Hamid 2008 Measurement of the slip length of water flow on graphite surface. *Applied Physics Letters* **92** (5), 053101.

Manica, Rogerio, Klaseboer, Evert & Chan, Derek YC 2016 The impact and bounce of air bubbles at a flat fluid interface. *Soft Matter* **12** (13), 3271–3282.

Manor, Ofer, Vakarelski, Ivan U, Tang, Xiaosong, O'Shea, Sean J, Stevens, Geoffrey W, Grieser, Franz, Dagastine, Raymond R & Chan, Derek YC 2008 Hydrodynamic boundary conditions and dynamic forces between bubbles and surfaces. *Physical review letters* **101** (2), 024501.

Masoud, Hassan & Stone, Howard A 2019 The reciprocal theorem in fluid dynamics and transport phenomena. *Journal of Fluid Mechanics* **879**.

Maxey, Martin R & Riley, James J 1983 Equation of motion for a small rigid sphere in a nonuniform flow. *The Physics of Fluids* **26** (4), 883–889.

Mo, Jianyong & Raizen, Mark G 2019 Highly resolved brownian motion in space and in time. *Annual Review of Fluid Mechanics* **51**, 403–428.

Otto, Florian, Riegler, Emmalee K & Voth, Greg A 2008 Measurements of the steady streaming flow around oscillating spheres using three dimensional particle tracking velocimetry. *Physics of fluids* **20** (9), 093304.

Redaelli, T, Candelier, F, Mehaddi, R, Eloy, C & Mehlig, B 2022 Hydrodynamic force on a small squirmer moving with a time-dependent velocity at small reynolds numbers. *arXiv preprint arXiv:2209.08138* .

Reynolds, Osborne 1886 Iv. on the theory of lubrication and its application to mr. beauchamp tower's experiments, including an experimental determination of the viscosity of olive oil. *Philosophical transactions of the Royal Society of London* (177), 157–234.

Rodríguez Matus, Marcela, Zhang, Zaicheng, Benrahla, Zouhir, Majee, Arghya, Maali, Abdelhamid & Würger, Alois 2022 Electroviscous drag on squeezing motion in sphere-plane geometry. *Phys. Rev. E* **105**, 064606.

Sader, John Elie 1998 Frequency response of cantilever beams immersed in viscous fluids with applications to the atomic force microscope. *Journal of applied physics* **84** (1), 64–76.

Shapiro, Ascher H, Jaffrin, Michel Yves & Weinberg, Steven Louis 1969 Peristaltic pumping with long wavelengths at low reynolds number. *Journal of fluid mechanics* **37** (4), 799–825.

Simha, Akarsh, Mo, Jianyong & Morrison, Philip J 2018 Unsteady stokes flow near boundaries: the point-particle approximation and the method of reflections. *Journal of Fluid Mechanics* **841**, 883–924.

Vakarelski, Ivan U, Manica, Rogerio, Tang, Xiaosong, O'Shea, Sean J, Stevens, Geoffrey W, Grieser, Franz, Dagastine, Raymond R & Chan, Derek YC 2010 Dynamic interactions between microbubbles in water. *Proceedings of the National Academy of Sciences* **107** (25), 11177–11182.

Villey, Richard, Martinot, Emmanuelle, Cottin-Bizonne, Cécile, Phaner-Goutorbe, Magali, Léger, Liliane, Restagno, Frédéric & Charlaix, Elisabeth 2013 Effect of surface elasticity on the rheology of nanometric liquids. *Physical review letters* **111** (21), 215701.

Wang, Shiyan & Ardekani, AM 2012 Unsteady swimming of small organisms. *Journal of Fluid Mechanics* **702**, 286–297.

Wang, Yuliang, Zeng, Binglin, Alem, Hadush Tedros, Zhang, Zaicheng, Charlaix, Elisabeth & Maali, Abdelhamid 2018 Viscocapillary response of gas bubbles probed by thermal noise atomic force measurement. *Langmuir* **34** (4), 1371–1375.

Wei, Da, Dehnavi, Parviz Ghoddoosi, Aubin-Tam, Marie-Eve & Tam, Daniel 2019 Is the zero reynolds number approximation valid for ciliary flows? *Physical review letters* **122** (12), 124502.

Wei, Da, Dehnavi, Parviz G, Aubin-Tam, Marie-Eve & Tam, Daniel 2021 Measurements of the unsteady flow field around beating cilia. *Journal of Fluid Mechanics* **915**, A70.

Zhang, Zaicheng, Arshad, Muhammad, Bertin, Vincent, Almohamad, Samir, Raphael, Elie, Salez, Thomas & Maali, Abdelhamid 2022 Contactless rheology of soft gels over a broad frequency range. *Phys. Rev. Applied* **17**, 064045.

Zhao, Cunlu, Zhang, Wenyao, van den Ende, Dirk & Mugele, Frieder 2020 Electroviscous effects on the squeezing flow of thin electrolyte solution films. *Journal of fluid mechanics* **888**.

van Zwieten, J.S.B., van Zwieten, G.J. & Hoitinga, W. 2022 Nutils 7.0.